Mon. Not. R. Astron. Soc. **000**, 1–12 (2010) Printed 15 January 2010 (MN LATEX style file v2.2)

Near-ground turbulence profiles from lunar scintillometer

A. Tokovinin*, E. Bustos, A. Berdja
Cerro Tololo Inter-American Observatory, Casilla 603, La Serena, Chile

-

ABSTRACT
A simple and inexpensive 6-channel array of photo-diodes, LuSci, can measure weak moonlight scintillation produced by optical turbulence within few hundred meters above the ground. We describe the instrument, its operation, and data reduction. Measured covariances of lunar scintillation are fitted to a smooth turbulence profile model with few parameters. Complete recipe for calculating the instrument response (including the effects of Moon's phases) is given. The robustness of the results relative to various experimental factors and model assumptions is investigated. We give examples of the data and compare LuSci with other turbulence profilers. LuSci finds numerous applications in night-time site testing and monitoring.

Key words: site testing – atmospheric effects

1 INTRODUCTION

Optical turbulence in the terrestrial atmosphere critically influences the capabilities of ground-based telescopes and interferometers. Atmospheric distortions can be partially corrected with Adaptive Optics (AO). Design and operation of AO systems and interferometers needs detailed information on the optical turbulence profiles (OTPs) and other parameters such as atmospheric time constant. New instruments are being developed and tested to answer this need.

A large fraction of optical turbulence is typically concentrated in the *surface layer* (SL) within a few hundred meters above the ground. At some sites, such as Dome C in Antarctica, the SL completely dominates the overall seeing. This is also true for day-time (solar) astronomy. It has been known since a long time (Codona 1986; Seykora 1993) that weak scintillation of extended sources such as the Sun or the Moon, *shadow bands*, is mostly produced in the SL. Beckers (2001) was the first to use this phenomenon for measuring the SL turbulence with an array of 6 detectors which record fast fluctuations of the solar flux. This instrument, called SHABAR, was used in the site survey for a modern solar telescope and played a decisive role in the final site selection (Socas-Navarro et al. 2005).

Moon can be used in a similar way to measure the night-time SL turbulence, as demonstrated by Hickson & Lanzetta (2004). A detailed analysis of this method was made by Kaiser (2004) in an unpublished report. A lunar scintillometer consists of an array of small detectors. Compared to SHABAR, the task of measuring and interpreting scintillation has some additional challenges (Moon's phases, smaller flux, etc.). Nevertheless, this method delivers robust estimates of OTP near the ground. In this paper, we study various instrumental and theoretical aspects of this technique.

A night-time SL turbulence monitor finds the following applications:

- Measuring the strength of the SL turbulence and its vertical distribution to predict the performance of ground-layer AO, as has been done e.g. for the Gemini-North telescope (Chun et al. 2009).
- Measuring the SL at new or existing sites to predict the seeing above a certain level or to determine the height of a telescope building.
- Translating the measurements of seeing obtained by a site monitor located in a small tower to the level of the telescope.

Compared to the standard technique of measuring the SL turbulence with micro-thermal probes, a lunar scintillometer, LuSci, has the advantage of being a direct optical method that is self-calibrated. It does not require a tower. Other optical methods for SL turbulence measurements are the SLODAR (Wilson et al. 2009) or the low-layer Scidar, LOLAS (Avila et al. 2008), but LuSci is much simpler. Obviously, LuSci works only when the Moon is above the horizon, which makes it unsuitable for continuous SL monitoring. It is appropriate for working in campaign mode or for calibrating other methods, e.g. micro-thermals or acoustic sounders.

We begin by describing the LuSci instrument in Sect. 2. The method of OTP restoration from the measured signals is developed and tested in Sect. 3. Examples of LuSci applications are given in Sect. 4, and conclusions in Sect. 5.

2 THE INSTRUMENT

2.1 Operational principle

The scintillometer consists of a linear array of photo-detectors pointed at the Moon (Fig. 1). Small fluctuations of the photocurrent are recorded with a time resolution of 2 ms during an accumulation time of the order of 1 min. Covariances between each pair of signals (i, j) are computed

* E-mail: atokovinin@ctio.noao.edu

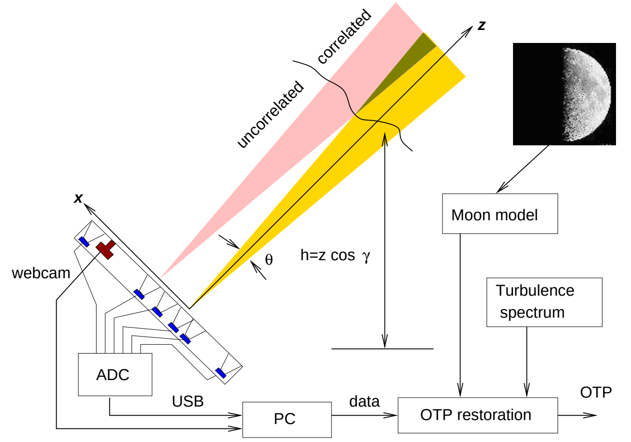

Figure 1. Block-diagram of the LuSci instrument. Fast fluctuations of moonlight are detected by 6 photo-diodes in linear configuration, digitized, and recorded in the computer. At large distances where the light cones from detector pairs overlap turbulence produces correlated signals, at shorter distances there is no correlation. The turbulence profile is determined by invoking models of turbulence spectrum and Moon's shape.

$$B_{i,j} = \frac{1}{K} \sum_{k=1}^{K} (\zeta_i \zeta_j)_k, \quad (1)$$

where $\zeta_i = I_i / \langle I_i \rangle - 1$ is the normalised fluctuation of the photo-current I_i at the detector i, K is the number of signal samples collected during the accumulation time.

Theory (Appendix A) relates the measured covariances to the distribution of the refractive-index structure constant $C_n^2(z)$ along the line of sight:

$$B(\boldsymbol{r}) = \int_0^\infty \mathrm{d}z \, W(\boldsymbol{r}, z) \, C_n^2(z). \quad (2)$$

The coordinate axis z is directed from the instrument to the Moon, and the transverse coordinates are $\boldsymbol{r} = (x, y)$. The *weighting functions* (WFs) $W(\boldsymbol{r}, z)$ are calculated from the known instrument parameters, Moon's image, and statistical turbulence model. The WFs are measured in $\mathrm{m}^{-1/3}$.

Given the set of measured covariances at a number of baselines r_l (including the zero baseline, i.e. the variance), Eq. 2 is inverted to infer the OTP $C_n^2(z)$. Practically, the OTP is represented by a smooth function of z with a small number of parameters which are fitted to the data.

2.2 Hardware

The scintillometer hardware should record small-amplitude fast fluctuations of the Moon's flux at several locations. Different engineering solutions are possible to do this. We assembled LuSci from cheap and readily available commercial components (Table 1). Copies of the instrument can be made with a minimal amount of in-house work.

Our instrument has evolved with time (e.g. Rajagopal et al. 2008). Here we describe its current version (Fig. 2). Six individual modules with photo-diodes and amplifiers are located inside the Π-shaped aluminium profile of $440 \times 102 \times 40$ mm size with a thin cover. The distances between the detectors (counting from the top) are $(0, 12, 15, 17, 21, 40)$ cm, forming a set of 15 non-redundant baselines from 2 cm to 40 cm. The method also works with smaller

Table 1. Commercial components of LuSci

Component	Vendor	Model	Qty
Photo-diode	thorlabs.com	FDS1010	6
Amplifier	Linear Technology	LT1464	6
8-channel ADC	cyberresearch.com	UMDAS 0802HR	1
Web camera 1/4"	logitech.com	Quickcam Pro 3000	1
Lens F=25mm	edmundoptics.com	NT56-776	1
Mount	celestron.com	NexStar 130-SLT	1

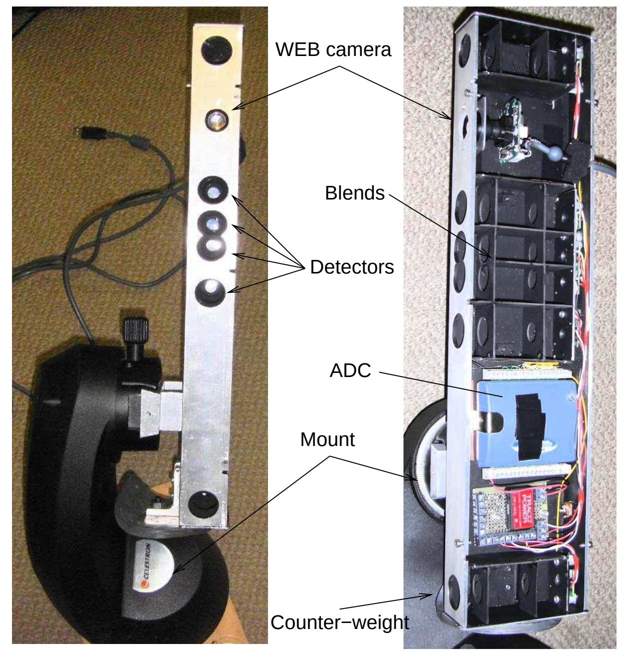

Figure 2. The 6-channel LuSci array fabricated at CTIO.

(four) or larger number of detectors. The choice of the configuration is motivated by the need to sample a range of baselines, form smallest to largest. Each detector is behind a circular aperture of 1 cm diameter. Baffling prevents grazed reflections from the walls and restricts the un-vignetted field of each detector to 10° diameter. Walls separate the light paths of individual detectors, except for the closest detector pair where the wall is shorter and the outer holes of 25.4-mm diameter partially overlap.

Signals from the detector modules are wired to the 8-channel, 16-bit analog-to-digital converter (ADC) housed in the same box. The ADC is connected to the personal computer (PC) via universal serial bus (USB), which also delivers the power. The power to the detector modules can be provided either from the $+5$ V USB line with an additional DC/DC converter, or by an external stabilised supply of ± 15 V. The box also contains a web-camera with a 25-mm lens, enabling remote pointing and tracking. The field of this camera/lens combination is about 10°.

The silicon photo-diodes FDS1010 have a square active area of $10 \times 10\,\mathrm{mm}^2$. The responsivity is around 0.65 A/W at 900 nm, with noise-equivalent power of 5.5×10^{-14} W Hz$^{-1/2}$ at this wavelength. We use the photo-diodes with zero bias voltage and transform the photo-current into voltage with a 9.1 MOhm resistor in the feedback loop (Fig. 3). The full Moon gives a photo-current of about 90 nA, or a signal voltage of about 1 V. The zero bias helps

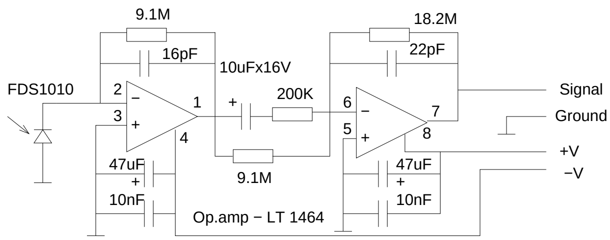

Figure 3. Electronic scheme of the detector module.

to maintain a low dark current (otherwise, at the nominal bias of -5 V the dark current of 600 nA is larger that the Moon's signal).

The relative fluctuations of the photo-current caused by scintillation can be as small as 10^{-4} (see below in Figs. 4,5). Direct digitisation of the signal with 16-bit resolution would be barely sufficient, provided that the full dynamic range of the ADC is used. This is why we separate the variable (AC) part of the signal above 0.1 Hz by a high-pass filter and amplify it by 90 times with the second stage before digitisation. However, the average (DC) level of the signal must be monitored as well. In the previous 4-channel versions of the instrument, we recorded the DC signal at the output of the first stage separately. This is not possible with 6 detectors and 8 ADC channels, therefore a small fraction of the DC signal is transmitted by the second stage. The ratio of the amplification coefficients of AC and DC parts $K_{\rm ampl} \approx 45$ is determined by the ratio of the resistors, then measured accurately to confirm, and used to re-normalise the fluctuations. Overall, the electronics behaves as though all fluctuations above 0.1 Hz were amplified by $K_{\rm ampl}$ times relative to the average signal level. Of course, all signal transients are amplified as well, so a stabilisation time of $\sim$30 s after pointing the Moon is needed before the measurements can start.

The ADC reads all channels sequentially at a rate of 5 kHz. The signals are averaged by the acquisition software to emulate the synchronous sampling of all channels at 500 Hz (10 reads in 2-ms time) and to average any rapid noise. Low-pass filtering in the amplifiers also helps to suppress noise outside the acquisition bandwidth. There was some concern that the large capacity of the unbiased photo-diode could smooth the signal. A direct test with faint light flickering at 110 Hz confirmed that the detector and its electronics behave like an RC-filter with a time constant $\tau = 0.36$ ms (3-dB bandwidth 440 Hz).

The amplifier partially transmits fluctuations of the supply voltages, therefore clean power and good grounding are essential. In the absence of light, the noise spectrum is flat, with typical rms around 0.3 mv in the 50-Hz bandwidth. This is close to the estimated Johnson noise of the 9-MOhm feedback resistor and less than the shot noise of the photon signal (0.9 mV for the full Moon). We estimate that the electronic and photon noises together contribute less than 1% to the variance of the scintillation signal.

2.3 Software and operation

The software to acquire signals and control the instrument is written in C++ and works under Windows. It was developed under Visual Studio 6.0. The configuration of the system is schematically shown in Fig. 1.

Parameters relevant to the operation and data acquisition are stored in a configuration file. They include geographical site coordinates, number of channels (six), sampling frequency, accumulation and averaging time, as well as technical data needed to acquire the signals and control the mount.

We do not rely on the pointing and tracking capability built into the mount and use it simply as a two-axis pointing device under computer control. The program calculates Moon's elevation and azimuth and points the instrument. The azimuth axis is aligned vertically at installation using the bubble level. The zero points in elevation and azimuth are set by powering the mount with the instrument pointed to the North. Small offsets are introduced to correct the pointing if necessary. As the required accuracy is only of few degrees, this procedure works well and permits a "cold start" of the mount remotely (without human presence) using inclination sensor and digital compass (or home switch) to initialise the pointing. The signals of those sensors are read through the free channels of the same ADC device.

The operation is controlled via a graphic user interface (GUI). Moon's image from the webcam is displayed to check or correct the pointing, if necessary. We are also developing an automatic tracking on webcam images.

At the start, the software offsets the pointing in altitude and/or azimuth to measure the sky background. The sky measurement is repeated after a certain number of Moon measures are collected. This way, we monitor the background and electronic offset, to be subtracted from the Moon's flux for proper normalisation of the covariances. Parameters defining the offsets and the numbers of Moon and sky measurements are read from the configuration file.

Segments of data of 5-s duration are acquired into the computer memory. Average values of signals, their variances and covariances are calculated and stored in a text file, together with the time stamp. The signal values are stored on the disk as unsigned 16-bit integers in another, binary file. Binary data can be accessed by means of a pointer which accompanies each text record. The text file is sufficient for calculating normalised covariances, but the binary data are used for off-line control: checking random and periodic noise, temporal power spectra and covariances. New text and binary files are opened each night.

The data saved on the disk are pre-processed by an IDL program which calculates the variances and covariances of the signals normalised by their average values, as required for the OTP restoration (Eq. 1). The sky level is subtracted from the measured fluxes and the AC/DC amplification coefficients are accounted for. The covariances are averaged over time (usually 1 min) and written to another file. The same program filters the data, removing erroneous measurements. The filtering algorithm approximates the flux in each channel by a polynomial as a function of time and removes measurements with flux deviations relative to the fit or flux fluctuations within 1 minute larger than 2%. Such data can be affected by clouds, pointing failures, etc. Other criteria to select valid data are low sky background (less than 5% of the Moon's flux) and sufficient number of valid 5-s data segments within each minute. For a normally operating instrument, the fraction of valid data in clear conditions is usually larger than 90%.

2.4 Tests

Various tests can be made to assure the good quality of the data. Temporal spectra calculated from the saved binary data usually show a smooth decline with frequency, spanning as much as 4 orders of magnitude (40 dB). In some instances there are narrow peaks caused either by electronic pickup noise (e.g. at 50 Hz) or by variable light sources which contribute to the flux (e.g. 100 Hz and harmonics from the street lights in the cities). No such peaks are

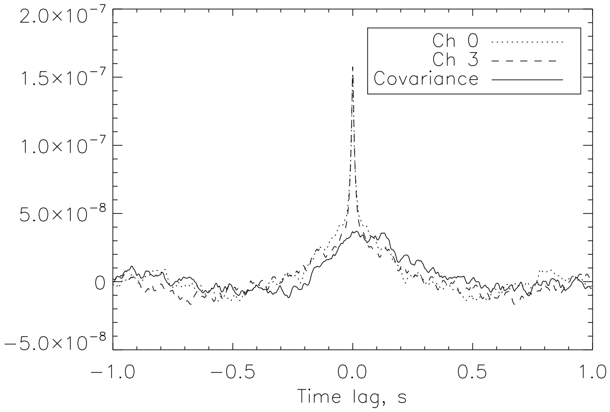

Figure 4. Temporal covariance between two detectors separated by 38 cm (full line) and auto-covariance of each detector (dotted and dashed lines). Data from Cerro Tololo, February 5, 2007. The distance between the detectors was 0.38 m.

seen in the data acquired in the LuSci campaigns at various observatories. The temporal power spectra of the dark noise are flat.

Figure 4 shows the temporal auto-covariance functions of two channels and their mutual covariance. The signal variance in all 6 channels is equal to better than 5%, showing that the amplification coefficients and flux normalisation are correct. The mutual covariance is wider than the auto-covariance, and its maximum is displaced from the coordinate origin by the transit time of shadow bands moving with the projected wind speed. Slow signal fluctuations also cause "wiggles" in the covariance and are the major source of statistical measurement errors (Appendix C). Wind velocity near the ground can be estimated by fitting a model to the temporal spectrum of the signal together with the measured OTP (Rajagopal et al. 2008).

The covariances decrease with the baseline, as plotted in Fig. 5. On February 6, 2009, this dependence was smooth, indicating that the SL turbulence was distributed over altitude. In contrast, the covariances decline very rapidly on February 12, showing that most of the SL turbulence was below 3 m.

3 PROFILE RESTORATION

Several approaches can be used to derive the OTP from measured covariances (inversion of Eq. 2). First, a simple linear method is outlined. It is replaced now by fitting data to a smooth OTP model with few parameters.

3.1 Weighting functions

The calculation of covariances and WFs is described in detail in Appendices A and B. The WFs do not depend on the wavelength, so there is no need to specify the spectral response of the instrument. At distances larger than 100 m, the WFs depend substantially on the turbulence outer scale L_0, which is usually not measured (we assume $L_0 = 25$ m). Figure 6 plots the WFs for LuSci (1-cm detectors, full Moon). Signals of a pair of detectors separated by baseline r become correlated at distances $z > r/\theta \sim 100r$ where the cones with Moon's angular diameter θ start to overlap (Fig. 1). At somewhat shorter distances, the covariance is slightly negative. The variance $B(0, z)$ falls down at $z < 3$ m because of the finite detector size.

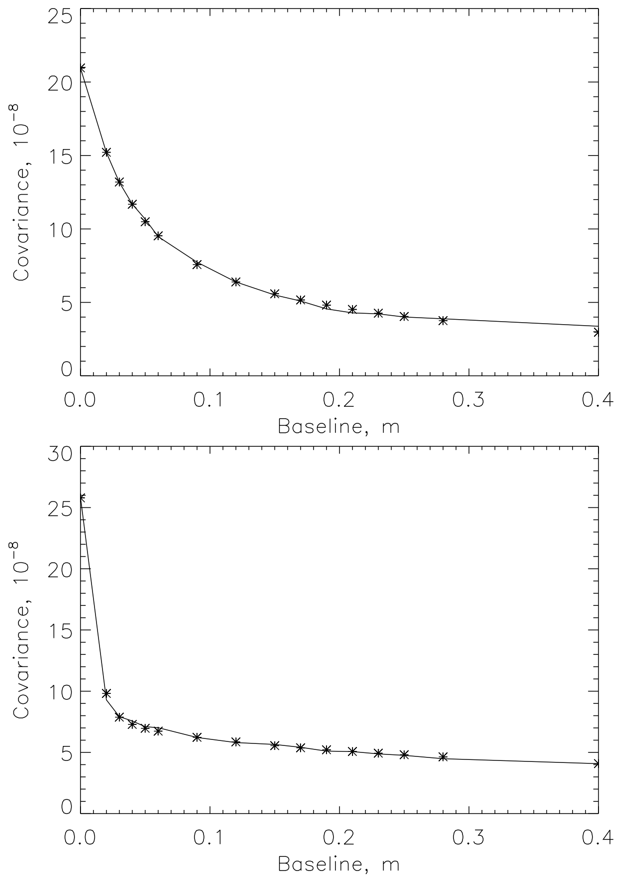

Figure 5. Covariances measured at Paranal averaged over one night are plotted versus baseline in full lines for the nights of February 6, 2009 (top panel) and February 12, 2009 (bottom panel). The asterisks show averaged covariances calculated from the fitted OTP models.

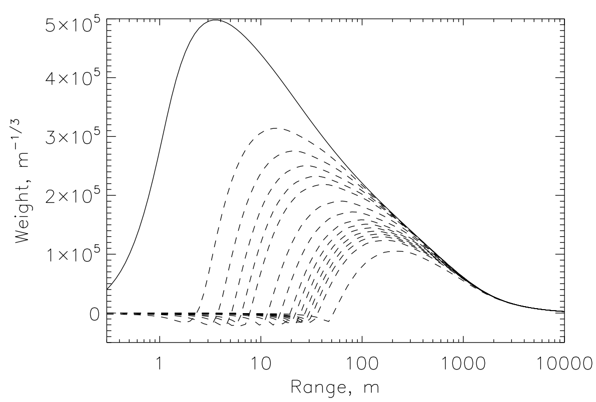

Figure 6. Weighting functions $W(z)$ for the 6-element array and full Moon. Full line – variance, dashed lines – covariances for baselines from 2 cm to 40 cm.

Averaging of scintillation by a detector of diameter d can be neglected for $z \gg d/\theta$, in which case the transverse scale of the covariance is determined only by the projected Moon's diameter, $r \sim \theta z$. As shown by Kaiser (2004), the change of variables from (r, z) to $(\log r, \log z)$ reduces the integral (2) to a simple convolution. It is natural to use the logarithmic grid in z for calculations of the WFs and for restoration of the OTP. The resolution $\Delta z/z$

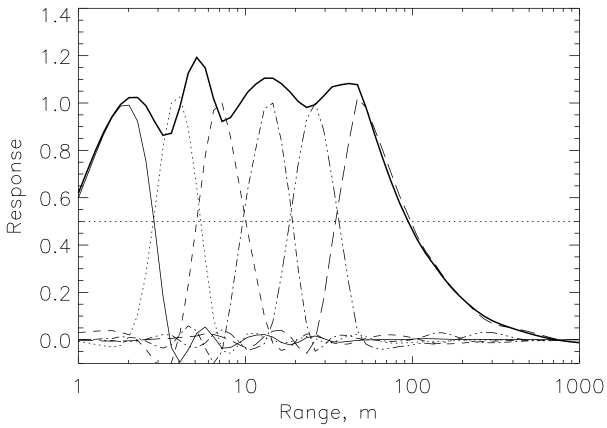

Figure 7. A set of response functions $R(z)$ for the 6-element array. The thick full line shows the sum of all response functions.

should be approximately constant. In this respect, LuSci differs from SLODAR, where the vertical resolution Δz is constant.

3.2 Linear restoration

It can be guessed from Fig. 6 that a difference between two covariances at bases r_1 and r_2 will provide information on turbulence located between r_1/θ and r_2/θ because the difference of the corresponding WFs will peak in this range. The idea can be developed further by finding linear combinations of covariances having near-constant response over some range and near-zero response outside it. Such combinations can be interpreted as integrals of C_n^2.

We define a logarithmic distance grid of $N = 100$ points from $z = 0.3$ m to 10 km. The fractional step $\epsilon_z = z_{n+1}/z_n = 1.11$ is fine enough to capture the details of the WFs. The OTP is represented by the n-element vector C of C_n^2 values on this grid, the WFs – as a matrix W of size $L \times N$, where L is the number of measured covariances B. In this discrete formulation, the integral (2) is replaced by a matrix product

$$\mathsf{B} = \mathsf{W}'\mathsf{C}, \quad \mathsf{W}'_{l,n} = W(r_l, z_n)\epsilon_z z_n. \tag{3}$$

Any linear combination of the WFs with coefficients $\mathsf{A} = \{a_l\}$ corresponds to the OTP integral J_R with some *response function* $R(z)$,

$$J_R = \sum_{l=1}^{L} a_l B_l = \int_0^\infty \mathrm{d}z\ R(z)\ C_n^2(z), \tag{4}$$

where

$$R(z) = \sum_{l=1}^{L} a_l W(r_l, z), \quad \text{or} \quad \mathsf{R} = \mathsf{W}^T \mathsf{A}. \tag{5}$$

We can find linear combinations of WFs which approximate some desirable responses. The mathematical details are omitted for brevity because this method is only of historic and didactic interest. It was used in the early LuSci campaigns (Thomas-Osip et al. 2008). Figure 7 gives an example of response functions for the 6-element array.

The simplicity of this linear method is appealing. The integrals J_R are calculated directly as weighted sums of the measured covariances. However, these integrals are defined along the line of sight, making it difficult to account for the zenith angle γ. If turbulence in the SL is concentrated in thin layers, the measured J should be multiplied by $\cos\gamma$ in order to reduce them to the zenith. On the other hand, if $C_n^2(z) = \mathrm{const}$, the integrals do not depend on γ. To complicate things further, the response functions R depend on the Moon's phase and baseline orientation. Therefore, the linear method is now replaced by model fitting.

3.3 OTP restoration by model fitting

Representing a continuous unknown OTP by a coarse model with few parameters is a kind of regularisation necessary to solve the inverse problem. One does not expect a miracle, i.e. that the model would render accurately any profile. Instead, we hope that the model will reproduce correctly the total intensity of turbulence and its location. The experience of site testing with SHABAR (Socas-Navarro et al. 2005) shows that individual OTPs are not very useful, as they contain excessive information. What is really needed usually is the measurement of turbulence integrals over specific ranges within the SL.

The OTP model is specified as a set of $C_n^2(Z_k)$ values at $K = 5$ fixed *pivot points* $Z_k = (3, 12, 48, 192, 768)$ m (here we refer to the 6-channel array). To enforce the non-negativity of the OTP, the model parameters are $Y_k = \log_{10} C_n^2(Z_k)$. Values between the pivot points are calculated by linear interpolation of Y_k on the logarithmic distance grid. This is equivalent to representing the OTP by power-law segments. Below Z_1 and above Z_5 the model OTP is extrapolated by constants equal to its values at the first and last pivot points.

Linear interpolation is expressed in the compact form by introducing the $N \times K$ matrix T of triangular functions:

$$T_k(z_n) = 1 - |\log_{10}(z_n/Z_k)|/\log_{10}(4) \tag{6}$$

for $|\log_{10}(z_n/Z_k)| < \log_{10}(4)$ and zero otherwise. This formula takes advantage of the fact that $Z_{k+1}/Z_k = 4$. Knowing the vector of model parameters Y, the OTP is calculated simply as

$$\log_{10} \mathsf{C} = \mathsf{T}\mathsf{Y}. \tag{7}$$

This corresponds to the model covariances $\hat{\mathsf{B}} = \mathsf{W}'\mathsf{C}$. We fit model to the measurements by minimising the χ^2 metric

$$\chi^2 = \frac{1}{L} \sum_{l=1}^{L} [(B_l - \hat{B}_l)/B_0]^2 + \beta S, \tag{8}$$

where the OTP smoothness S is defined as

$$S = \sum_{k=2}^{K-1} |Y_k - 0.5(Y_{k-1} + Y_{k+1})|. \tag{9}$$

The rationale for this metric is as follows. First, we normalise the residuals simply by the measured variance B_0 rather than by the estimated measurement errors of B_l because these errors are not known, they are mutually correlated and of comparable magnitudes (Appendix C). Second, we add a smoothness penalty with the regularisation parameter $\beta = 10^{-4}$. If the restored OTP has a spike of 1 dex (i.e. 10 times), the typical χ^2 will increase by 25%. Regularisation helps to select the smoothest solution among many solutions compatible with the data.

If an OTP is represented by linear (rather than power-law) segments between the pivot points, the values at these points can be found immediately because the unknowns and data are related to each other linearly. However, the non-negativity and smoothness of the OTP are not guaranteed. The linear model serves to find preliminary values of Y_k which are then used as a starting point in

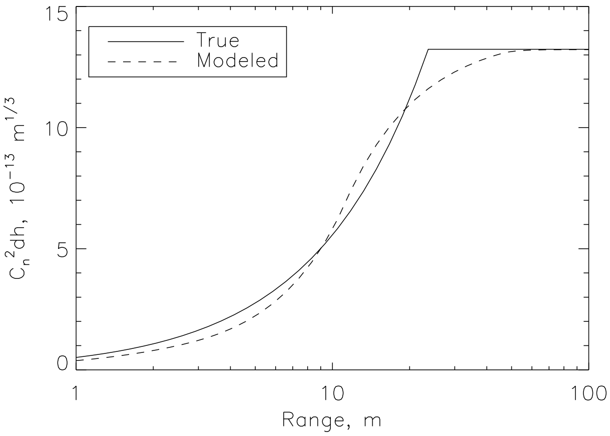

Figure 8. Test of modelling errors. The input OTP abruptly changes from $5\,10^{-14}$ to 10^{-18} m$^{-2/3}$ at 24 m. Its integral is plotted in the full line. The integral of the model OTP fitted to the covariances is plotted in dashed line.

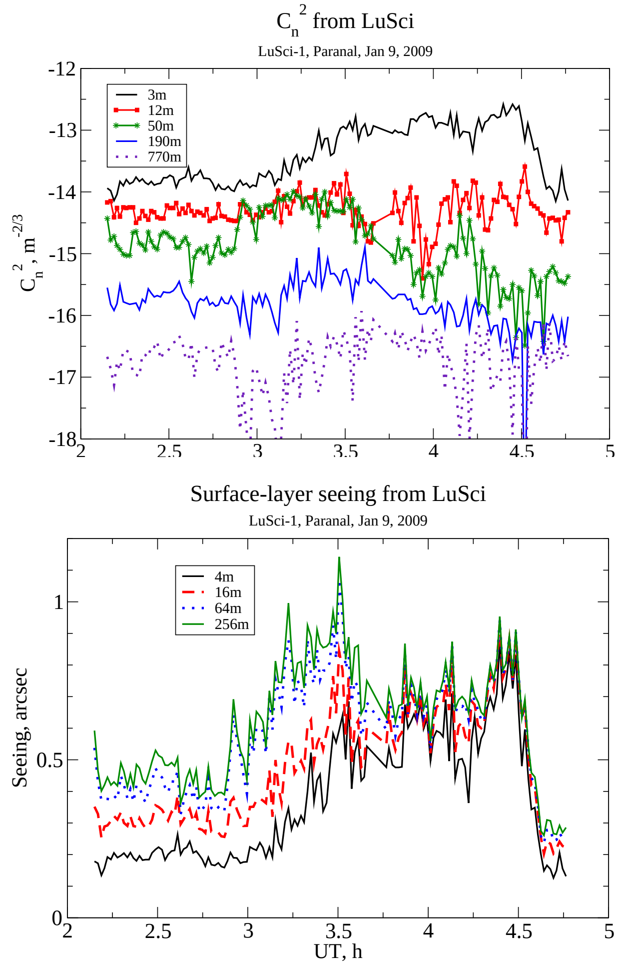

Figure 9. Results of the OTP measurement on the night of January 9/10, 2009 at Paranal. The C_n^2 values at 5 pivot points are plotted as a function of time on the upper panel. The lower panel shows seeing in the SL (at 500 nm at zenith) integrated from the instrument to the heights of 4, 16, 64, and 256 m calculated from these OTPs.

the minimisation of (8). An even better choice is to use the previously measured OTP (when available) as a starting point. The minimisation is done with the AMOEBA method (Press, Flannery, & Teukolsky 1986). Typically, $\chi^2 \sim 0.02^2$ is reached (see asterisks in Fig. 5).

The OTP model consisting of power-law segments can reproduce very well smooth profiles such as exponential. When the OTP changes abruptly, e.g. from high to low level, the fitted model is necessarily inaccurate. Even in this worst-case situation (Fig. 8) the turbulence integrals are recovered with errors less than 10%. When we add to all covariances a large constant to emulate the effect of transparency fluctuations, the dashed curve in Fig. 8 remains practically unchanged (the constant offset is absorbed by increasing the last Y_k without affecting values at other pivot points). However, the fitted model under-estimates turbulence integrals for very steep OTPs because it does not allow for strong turbulence in the immediate vicinity of the instrument. For example, for an OTP $C_n^2(h) \propto h^{-2.5}$ the estimated SL integral is only 0.6 of its true value. Nevertheless, C_n^2 above 3 m is measured correctly. This bias can be easily fixed by adding another pivot point at 0.75 m.

The data product of LuSci is a text file. Each line contains the Julian date of the measurement, air mass $\sec\gamma$, SL seeing, and fitting error χ^2. Then the values of Y_k are listed, followed by the turbulence integrals up to several user-defined heights. Turbulence integrals over any height interval (h_1, h_2) can be easily calculated from Y_k. To do this, we take the Z_k listed at the beginning of the file, compute the matrix T on a fine logarithmic z-grid and use (7) to reconstruct the OTP. The integral is found by summing up $C_n^2(z_i)\Delta z_i$ in the interval between $h_1 \sec\gamma$ and $h_2 \sec\gamma$ and multiplying the result by $\cos\gamma$. The piece-wise power-law OTP can also be integrated analytically.

A variant of the pivot-points method has been used in processing the SHABAR data (Socas-Navarro et al. 2005). On the other hand, Hickson, Pfrommer & Crotts (2008) fitted scintillation covariances to an OTP model consisting of two decaying exponents. This imposes an additional constraint on the modeled OTP which can only decrease with height.

3.4 Robustness of LuSci results

Consistency. Figure 9 shows an example of the OTPs measured during one night. A general tendency of turbulence decreasing with height is seen, but there are some exceptions. Note the slow variation of the model parameters with time. This shows that the restoration is not dramatically affected by the random noise and that the two OTPs measured within one minute from each other are similar.

Sky background measured by offsetting the instrument is under-estimated because the sky around the Moon is brighter. This leads to under-estimating measured covariances and C_n^2 by a factor $(1-\epsilon)^2$, where ϵ is the fraction of the Moon's flux scattered by the sky in the 10° instrument field and unaccounted for by the sky measurements. The scattered light cannot exceed the total extinction, so we can safely assume that $\epsilon < 0.1$. The bias can possibly be removed by modeling the sky brightness around the Moon, for now we estimate that it is $< 20\%$.

Choice of the pivot points is not critical. Average OTP at a given site shows a smooth dependence on height, without any details near Z_k. We tried OTP restoration with different sets of Z_k and obtained very similar results. A version of the algorithm using six Z_k with a ratio of 3 (rather than 4) also works well.

Temporal filtering of the scintillation signal can cause under-estimation of near-ground turbulence. This effect becomes important when $V\tau/\max(z\theta, d)$, the ratio of the wave-front translation

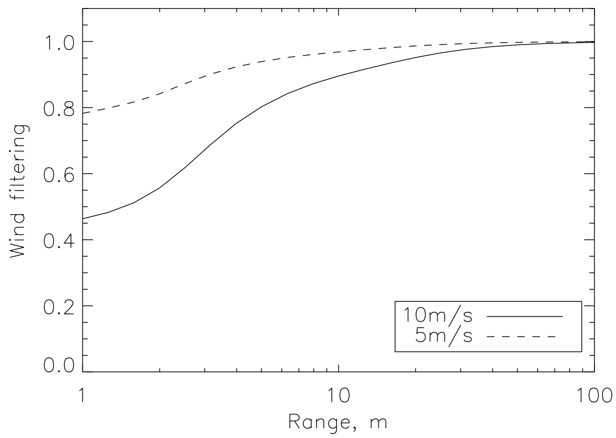

Figure 10. Reduction of scintillation variance in 1-cm aperture for wind speeds of 5 m/s and 10 m/s, wind direction perpendicular to the terminator, 8 days after new Moon.

during exposure time $\tau = 2$ ms by the transverse wind speed V to the spatial scale of scintillation, becomes comparable to one or larger. Maximum effect is observed on the variance $B(0)$.

The temporal filtering is evaluated by including additional factor in the calculation of the WFs (Appendix B). The ratio of filtered to un-filtered scintillation variance is plotted in Fig. 10 for the worst-case scenario: 8 days after new Moon, wind direction perpendicular to the terminator. In this case, C_n^2 can be under-estimated by as much as 2 times at close distances, but the effect is small at $z > 10$ m. For the full Moon or other wind directions the temporal bias is even less. When the ground wind speed is known, we account for it in the calculation of the WFs.

Slow signal fluctuations are not passed by the low-cutoff filter (0.1 Hz) and are further suppressed by calculating the covariances on 5-s signal segments. Slow scintillation signal originates at large distances. The 5-s segments correspond to spatial samples of 50 m (for wind speed 10 m/s), so any missed low-frequency signal is correlated in all detectors. Small variations of atmospheric transparency cause the opposite effect: all covariances are increased by same unknown amount.

We evaluated the influence of additive bias on covariances (either positive or negative) by numerical simulation. It changes the C_n^2 values at the highest pivot point. All WFs at $z > 700$ m are essentially identical (Fig. 6), so the bias is interpreted by the fitting algorithm as high-altitude turbulence and accounted for by adjusting the last Y_k. However, this has little influence on the remaining pivot points. The OTP at $z < 200$ m measured by LuSci is stable against additive biases in the covariances.

Finite turbulence outer scale L_0 influences the WFs at large distances $z > L_0/(2\pi\theta) \sim 40$ m (for typical $L_0 = 25$ m). The effect is essentially the same on all WFs. Changes of adopted L_0 affect only the last Y_k, like additive bias on covariances. Taken together, the unknown outer scale, transparency variations, and high-pass temporal filtering conspire to compromise measurements of high-altitude turbulence by LuSci. For the same reason, it makes little sense to increase the baseline beyond 0.4 m. Attempts to relate lunar or solar scintillation signal to the total atmospheric seeing have been made (Beckers 2001; Hickson, Pfrommer & Crotts 2008), but other methods of seeing measurements like DIMM are much more reliable. In joint fitting of SHABAR data and seeing, the outer-scale effect had to be modeled by an additional free parameter, “missing scintillation” (Socas-Navarro et al. 2005). In the case of LuSci, we do not attempt to measure the total seeing.

Kolmogorov turbulence spectrum underlines the definition of C_n^2, the interpretation of scintillation in terms of this parameter, and its further use in evaluating seeing or AO performance. As this model is only a first approximation of the atmospheric distortions, all results are necessarily model-dependent and approximate as well. This circumstance is often forgotten. Strictly speaking, C_n^2 cannot be defined locally because the model assumes stationarity. We also neglect the anisotropy of the turbulence spectrum, which can be substantial near the ground.

The spatial scale of optical distortions which produce lunar scintillation ranges from 1 cm to 1 m at distances from 1 m to 100 m. These scales encompass the range of the Fried’s r_0 values relevant to optical propagation. The validity of the Kolmogorov model in this restricted range is of little doubt, while potential deviations of the power-spectrum index from its canonical value $-11/3$ will have only a mild effect. In contrast, extending the measurement range to smaller or larger scales increases the sensitivity to the turbulence model. For this reason, LuSci uses 1-cm detectors and makes no attempt to measure turbulence very close to or very far from the instrument.

Optical propagation is usually treated in the small-perturbation approximation (Tatarskii 1971; Roddier 1981). Situations where this approximation fails are not uncommon. For example, interpretation of stellar scintillation in the MASS instrument fails for scintillation indices above 0.6 and requires semi-empirical corrections otherwise (Tokovinin & Kornilov 2007). Fortunately, lunar scintillation is described by the geometric optics and is so small (so far from the focusing regime) that the small-perturbation theory works perfectly (Kaiser 2004). Therefore, the relation of the LuSci signal to C_n^2 is very well defined. The signal itself is just a flux variation. LuSci does not need any calibration and measures the C_n^2 on absolute scale. It is a good method to calibrate other, less direct techniques of turbulence profiling.

4 SOME RESULTS

Several LuSci instruments have been fabricated by ESO for the site selection program of the future European 42-m telescope, E-ELT. In 2008-2009, these lunar scintillometers were extensively tested at the Paranal observatory in Chile together with other instruments.

The SLODAR turbulence profiler (Wilson et al. 2009) was modified to measure the SL turbulence with increased resolution (Osborn et al. 2010) and operated at Paranal simultaneously with LuSci in February and April 2009 by J. Osborn and H. Shepherd. Wide binaries were observed to measure the OTP up to ∼60 m height, in 8 equally spaced bins. In Fig. 11 we compare the turbulence integrals $J_{\rm SLODAR}$ and $J_{\rm LuSci}$ from 6 m height above ground to the upper limit of SLODAR range (which varied from 52 m to 78 m, mean 65 m) calculated from the SLODAR and LuSci data matched in time to within 1 min. This comparison avoids the first few meters affected by the strong local turbulence. The medians of 2096 integrals are $0.64\,10^{-13}$ and $0.47\,10^{-13}$ m$^{1/3}$ for SLODAR and LuSci, respectively. These median values correspond to $\sim 0.2''$ seeing, so at Paranal the SL turbulence above 6 m is typically weak. Large scatter between the two instruments is caused mostly by statistical difference of turbulence which they sample on different paths, rather than by measurement errors. The systematic difference (LuSci integrals are smaller by 30%) is likely explained by the fact that SL at Paranal is slightly tilted. The SLO-

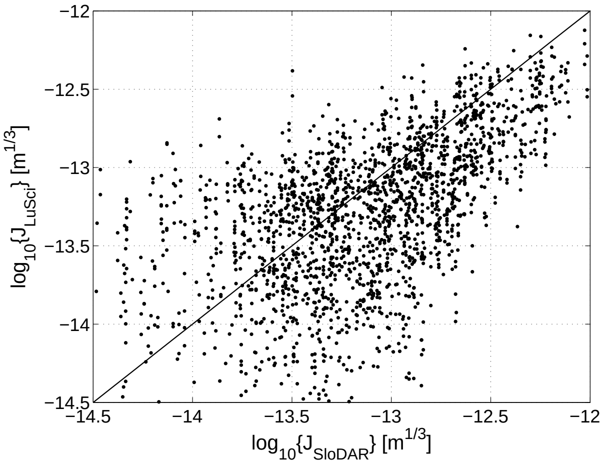

Figure 11. Comparison between turbulence integrals measured simultaneously with LuSci and SLODAR at Paranal.

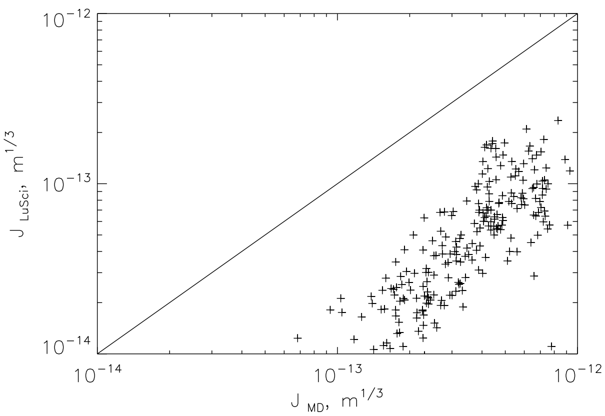

Figure 12. Comparison of turbulence integrals in the ground layer measured simultaneously by the MASS-DIMM instrument and LuSci at Paranal in February 2009.

DAR observed mostly stars in the southern part of the sky, LuSci was pointed to the Moon in the North. A small, but significant trend of the ratio $\log(J_{\rm LuSci}/J_{\rm SLODAR})$ with the difference in air mass between the instruments supports this explanation.

Integrated turbulence strength in the ground layer is deduced by the difference between turbulence integrals measured with the DIMM and MASS instruments (Tokovinin & Kornilov 2007). These integrals $J_{\rm MD}$ correspond to a response function which starts at 6 m above ground (the height of the site monitor) and smoothly falls to zero between 250 m and 500 m. We model this falling part as linear in height, but this assumption is not critical because $J_{\rm MD}$ is usually dominated by the first few meters. OTPs measured by LuSci were converted to turbulence integrals with the same response and compared to $J_{\rm MD}$. Figure 12 shows such comparison at Paranal for February 2009 (6 nights, 110 integrals averaged in common 5-min. intervals). The correlation and systematic difference are obvious, with median integrals $3.6\,10^{-13}$ and $0.41\,10^{-13}$ m$^{1/3}$ for the MASS-DIMM and LuSci, respectively. The MASS-DIMM measured turbulence almost an order-of-magnitude stronger than LuSci and SLODAR.

The difference between MASS-DIMM and LuSci at Paranal is not constant. For example, the median integrals are closer to each other in July 2009 (MASS-DIMM: $5.4\,10^{-13}$, LuSci: $2.6\,10^{-13}$ m$^{1/3}$). The difference becomes smaller or even changes sign when LuSci integrals are calculated from the instrument level up, rather than from 6 m above ground. Most likely, the Paranal site monitor is strongly affected by local turbulence, making wrong the default assumption that both instruments measure the same horizontally-stratified OTP. Systematic excess of the DIMM seeing compared to the seeing in the VLT is a known feature of the Paranal observatory (Sarazin et al. 2008). It is not our purpose here to investigate the SL at Paranal. The point is that the new instrument, LuSci, brings new insights.

5 CONCLUSIONS

Our experience with LuSci and the studies reported here show that this is a robust and cheap method to measure optical turbulence profile in the first 100–200 meters above night-time astronomical sites. The OTPs are self-calibrated and derived from the optical propagation – an obvious advantage over *in situ* microthermal probes. Compared to masts and towers, remote turbulence sounding by moonlight is non-intrusive; it does not create additional man-made turbulence and could help to detect such effects in other instruments. This will be particularly relevant at sites with excellent natural seeing, where even a small internal turbulence in a DIMM matters.

After testing at Paranal, the LuSci instruments will be used in the E-ELT site program. The Giant Magellan Telescope project also plans to use lunar scintillometers for characterising the SL. The first LuSci campaign at Las Campanas observatory with a 4-channel array gave encouraging results (Thomas-Osip et al. 2008). This early instrument also worked at Paranal in December 2007. The 12-channel lunar scintillometer built at the University of Vancouver is deployed at Cerro Tololo since 2006 to study the optimum height of future telescope domes (Hickson, Pfrommer & Crotts 2008). Our model-fitting was successfully tested on the data from this instrument, and a good agreement with our 6-channel array was found during the comparison campaign in March 2009.

A new exciting application of lunar scintillometers will be the study of intense surface turbulence at Arctic and Antarctic sites. The simplicity and robustness of this method are the key features in this application. Such instruments are being developed now.

ACKNOWLEDGEMENTS

The development of LuSci was stimulated by the current site-testing programs. M. Sarazin played a key role in our effort and helped in many different ways. Financial support to one of us (A.B.) from ESO is gratefully acknowledged. We thank P. Hickson for generously sharing his insights and technical information on the 12-channel instrument. Data from Paranal used here as examples were obtained by G. Lombardi. We thank J. Osborn for permission to use the SLODAR data in Fig. 11.

REFERENCES

Avila R., Avilés J. L., Wilson R. W., Chun M., Butterley T., Carrasco E. 2008, MNRAS, 387, 1511

Beckers, J.M. 2001, Exp.Astr, 12, 1

Bendat, J.S. & Piersol, A.G. Random Data. Analysis and measurement procedures. 1986, Wiley & Sons: New York.

Chun, M., Wilson, R., Avila, R., Butterley, T., Aviles, J.-L., Wier, D., & Benigni, S. 2009, MNRAS, 394, 1121
Codona, J.L. 1986, A&A, 164, 415
Hickson, P. & Lanzetta, K. 2004, PASP 116 1143
Hickson, P., Pfrommer, T., & Crotts, A. 2008, Proc. Conf. "Optical Turbulence: Astronomy meets Meteorology", Sardenia, Italy.
Kaiser, N., 2004, "Site evaluation using lunar shabar". Pan-STARRS internal memo, http://pan-starrs.ifa.hawaii.edu/project/events/talks/2004-01-23_kaiser.pdf
Kornilov, V., Tokovinin, A., Voziakova, O. et al., 2003, Proc. SPIE, 4839, 837
Osborn, J., Wilson, R., Butterley, T. & Shepherd, H. 2010, Profiling the turbulent surface layer with SLODAR (in preparation)
Press, W.H., Flannery, B.P., Teukolsky, S.A. 1986, Numerical Recipes: The Art of Scientific Computing (Cambridge Univ. Press)
Rajagopal, J., Tokovinin, A., Bustos, E., & Sebag, J. 2008, Proc. SPIE, 7013, paper 60
Roddier, F. in Progress in Optics, E. Wolf, ed., 19, p. 281, North-Holland, Amsterdam, 1981.
Sarazin, M, Melnick, J., Navarrete, J. & Lombardi, G. 2008 ESO Messenger, 132, 11
Seykora, E.J. 1993, Sol. Phys., 145, 389
Socas-Navarro, H., Beckers, J., Brandt, P. et al. 2005, PASP, 117, 1296
Thomas-Osip, J., Bustos, E., Goodwin M. et al. 2008, Proc. SPIE, 7014, paper 196
Tatarskii, V.I. 1971, The effects of the turbulent atmosphere on wave propagation. Nat. Tech. Inform. Service, Springfield, VA.
Tokovinin, A. & Kornilov, V. 2007, MNRAS, 381, 1179
Wilson, R.W., Butterley, T., & Sarazin, M. 2009, MNRAS, in press.

APPENDIX A: WEIGHTING FUNCTIONS

Here we give the recipe for calculating the weighting functions (WFs) which relate OTP with measured covariances (Eq. 2). Similar derivations can be found in (Codona 1986; Kaiser 2004; Hickson & Lanzetta 2004).

Standard theory of optical propagation through turbulence (Tatarskii 1971; Roddier 1981) provides expression for the spatial power spectrum of light amplitude at the ground created by a thin turbulent layer at a distance z:

$$\Phi_\chi(\boldsymbol{f}, z) = \alpha(2\pi)^2 \lambda^{-2} f^{-11/3} C_n^2(z) \mathrm{d}z \ \sin^2(\pi \lambda z f^2). \tag{A1}$$

The origin of the coordinate system is at the observer, the axis z is directed towards the light source, other coordinates x, y are in the wave-front plane, corresponding to the 2-dimensional spatial frequency vector $\boldsymbol{f} = (f_x, f_y)$ and $f = |\boldsymbol{f}|$. The light source is monochromatic with wavelength λ, local turbulence strength is $C_n^2(z)\mathrm{d}z$, the numerical coefficient $\alpha = 0.00969$. This equation is valid only for small amplitude fluctuations $\chi = \log[E(x,y)/\langle E \rangle] \ll 1$. To account for the finite outer scale L_0, additional multiplier $[1+(f/L_0)^2]^{-11/6}$ must be included in (A1).

For an extended incoherent source such as Moon, scintillation patterns produced by different source elements superimpose, leading to a convolution with the projected source image $A(x, y, z)$. For example, a uniform disk of angular diameter θ projects to a circle of diameter θz and creates the spatial filter

$$\tilde{A}(f, z) = 2 J_1(\pi f \theta z)/(\pi f \theta z), \tag{A2}$$

where J_1 is the Bessel function. By definition, the filter is normalised so that $\tilde{A}(0) = 1$. Filtering by the source and detector of diameter d limits the effective spatial frequencies to $f < 1/\max[\theta z, d]$. For the Moon's diameter $\theta \sim 10^{-2}$ rad, the argument under the sine in (A1) is always $\ll 1$. In other words, the Fresnel radius $\sqrt{\lambda z}$ is always much smaller than the projected source diameter θz or the detector size d. Replacing sine with its argument and going from amplitude fluctuations to intensity fluctuations, $W_\zeta = 4 W_\chi$ (here $\zeta(x, y)$ is the normalised intensity fluctuation, $\zeta = I/\langle I \rangle - 1$), we get

$$\Phi_\zeta(\boldsymbol{f}, z) = \alpha(2\pi)^4 f^{1/3} P_A(\boldsymbol{f}, z) \, C_n^2(z) \mathrm{d}z, \tag{A3}$$
$$P_A(\boldsymbol{f}, z) = |\tilde{A}(\boldsymbol{f}, z)|^2. \tag{A4}$$

This is the geometric-optics approximation where intensity fluctuations are produced by the local curvature of the wave-front,

$$\zeta(x, y) = z \nabla^2_{xy} \eta(x, y, z) \odot A(x, y, z), \tag{A5}$$

$\eta(x, y) = \lambda/(2\pi) \, \varphi(x, y)$ being the wave-front distortion, $\varphi(x, y)$ the phase, and ∇^2_{xy} the Laplacian operator over x, y. The intensity fluctuations are achromatic. The approximation of small perturbations which is essential in (A1) can now be dropped because, as demonstrated by Kaiser (2004), the intensity fluctuations from an extended source remain very small and Eq. A3 is still valid even when the point-source scintillation is strong, $\chi \sim 1$. The validity of (A3) under strong scintillation is readily proved by numerical simulation. When $\chi \sim 1$ for a point source, the light is focused at spatial scales of the order of Fresnel radius $\sqrt{\lambda z}$ or smaller. For an extended source, these fluctuations are averaged out on larger scales, where the small-perturbation theory remains valid.

The last step in the derivation of the WFs is to combine the scintillation spectra produced by all turbulent layers, assumed to be statistically independent. This leads to

$$\Phi_\zeta(\boldsymbol{f}) = \alpha(2\pi)^4 \, f^{1/3} \, [1+(f/L_0)^2]^{-11/6} \times \int_0^\infty \mathrm{d}z \, z^2 \, C_n^2(z) \, P_A(\boldsymbol{f}, z). \tag{A6}$$

The outer-scale factor is included here. The intensity covariance at baseline $\boldsymbol{r} = (x, y)$ is calculated by the Fourier transform (FT) of (A6),

$$B_\zeta(\boldsymbol{r}) = \langle \zeta(\boldsymbol{r}' + \boldsymbol{r}) \, \zeta(\boldsymbol{r}') \rangle = \int \mathrm{d}^2 \boldsymbol{f} \; \Phi_I(\boldsymbol{f}) \exp(2\pi i \boldsymbol{r} \boldsymbol{f}). \tag{A7}$$

By changing the order of integration, we finally obtain the formula for calculating the WF,

$$W(\boldsymbol{r}, z) = \alpha(2\pi)^4 \int \mathrm{d}^2 \boldsymbol{f} \; f^{1/3} [1+(f/L_0)^2]^{-11/6} \times P_A(\boldsymbol{f}, z) \exp(2\pi i \boldsymbol{r} \boldsymbol{f}). \tag{A8}$$

The spatial filter $P_A(\boldsymbol{f}, z)$ combines the convolutions with the source image and detector averaging. It may also account for the finite exposure time, as detailed in the next Section. If there were no $f^{1/3}$ factor under the integral, the scintillation covariance would be simply proportional to the auto-correlation of the source. In fact it resembles the source auto-correlation and falls to zero at $r > \theta z$, with some negative "ringing".

When going from (A3) to (A6), we made the usual assumption that turbulence can be represented by a combination of independent phase screens. This is not a very good approximation in the case of LuSci where the transverse distance r can be of the same order as the propagation distance z. We repeated the derivation of the spectrum of intensity fluctuations starting from the geometric-optics formula (A5) integrated along the line of sight,

$$\zeta(x,y) = \int_0^\infty \mathrm{d}z\, z\, \nabla^2_{xy} n(x,y,z). \tag{A9}$$

The FT over coordinates x, y is taken and the spatial variations of the air refractive index $n(x,y,z)$ are related to the 3-dimensional spatial spectrum of refractive-index fluctuations

$$\Phi_n(\boldsymbol{\kappa}) = \langle |\tilde{n}(\boldsymbol{\kappa})|^2 \rangle = \alpha C_n^2(z) |\boldsymbol{\kappa}|^{-11/3}, \tag{A10}$$

where $\boldsymbol{\kappa}$ is the 3-dimensional spatial frequency. The Kolmogorov turbulence model assumes isotropic and spatially stationary random process. By allowing the dependence $C_n^2(z)$, we formally commit an error. An attempt to constrain or measure C_n^2 locally violates the statistical model which defines this parameter! Therefore, the theory can be approximately valid only in situations where the dependence of C_n^2 on coordinates is smooth, on length scales much larger than the spatial scales of the problem.

We do not reproduce here the full derivation, which leads to the same formula (A6) where only $P_A(\boldsymbol{f}, z)$ is replaced by a slightly modified spatial filter

$$\begin{aligned} P'_A(\boldsymbol{f}, z) &= fz \int_{-1}^{+1} \mathrm{d}\epsilon\, Y(\epsilon f z)\, (1-\epsilon^2) \\ &\times \tilde{A}[\boldsymbol{f}, z(1+\epsilon)] \tilde{A}^*[\boldsymbol{f}, z(1-\epsilon)]. \end{aligned} \tag{A11}$$

The function $Y(x)$ is defined as

$$\begin{aligned} Y(x) &= \textstyle\int_{-\infty}^{+\infty} \mathrm{d}a (1+a^2)^{-11/6}\, \mathrm{e}^{2\pi i a x} \\ &\approx 1.68\, \exp[-5.55 x^2/(x+0.24)] \end{aligned} \tag{A12}$$

It is symmetric, falls exponentially to zero for arguments larger than one, and its integral equals 1. The numerical approximation in (A12) is accurate to better than 0.5%.

Analytical arguments and numeric calculation show that the difference between the exact filter (A11) and its approximation (A4) is small. The Moon filtering means that the spatial frequencies $f \sim (\theta z)^{-1}$ mostly contribute to the scintillation. The function Y falls off rapidly, and the integrand is substantially non-zero for $\epsilon f z < 1$, which leads to $\epsilon < \theta \sim 0.01$. Therefore, averaging of the spatial filter in (A11) occurs over a 1% fraction of the propagation distance and can be neglected. Some difference is found only at very low spatial frequencies where $zf \sim 1$, i.e. at spatial scales comparable to the propagation distance, but these scales make no effect on scintillation.

APPENDIX B: MOON MODELS

The aperture filter function in (A8) is a product of factors corresponding to the Moon's image and detector. Let $O(\xi, \eta)$ be the angular intensity distribution in the Moon's image, then

$$\begin{aligned} \tilde{A}_{\rm Moon}(f_x, f_y, z) &= \left[\textstyle\int \mathrm{d}\xi \mathrm{d}\eta\, O(\xi,\eta)\right]^{-1} \textstyle\int \mathrm{d}\xi \mathrm{d}\eta\, O(\xi,\eta) \\ &\times \exp[2\pi i z (f_x \xi + f_y \eta)]. \end{aligned} \tag{B1}$$

For a circular detector of diameter d, the filter does not depend on z and equals

$$\tilde{A}_{\rm det}(f) = 2 J_1(\pi f d)/(\pi f d). \tag{B2}$$

The full filter is

$$P_A(\boldsymbol{f}, z) = |\tilde{A}_{\rm Moon}(\boldsymbol{f}, z)|^2\, |\tilde{A}_{\rm det}(\boldsymbol{f})|^2\, P_{\rm wind}(\boldsymbol{f}, z). \tag{B3}$$

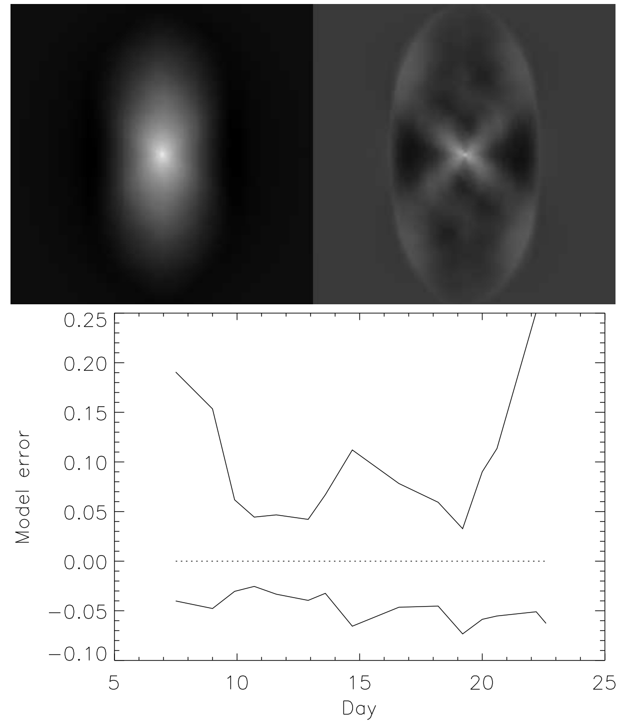

Figure B1. The top panel shows the scintillation covariance calculated for the true Moon's image at $t_M = 7.5\,$d and its re-scaled difference with the ellipse model. The low panel plots the maximum and minimum model errors $E = [B_{\rm ell}(\boldsymbol{r}) - B_{\rm Moon}(\boldsymbol{r})]/B_{\rm Moon}(0)$ as a function of the Moon's age t_M.

The multiplier $P_{\rm wind}(\boldsymbol{f}, z) = {\rm sinc}^2[\boldsymbol{V}(z)\boldsymbol{f}\tau]$ accounts for the averaging of scintillation signal during finite sampling time τ. Here $\boldsymbol{V}(z)$ is the vector of the ground wind speed and ${\rm sinc}(x) = \sin(\pi x)/(\pi x)$.

In principle, it is possible to use a collection of Moon's images in different phases and, for each observation, select the best match in phase for calculating the WFs or interpolate. This approach appeared too heavy, so we sought to approximate the Moon's filter. It turns out that a uniformly illuminated ellipse can serve to calculate the scintillation covariance to better than 10%. A more sophisticated *matrix model* gives an even smaller error.

B1 Ellipse model

We used the collection of Moon's images with daily sampling of phases posted by T. Talbott[1]. The original 800-pixel images were re-scaled and re-binned on a 128^2 square grid in such way that the image diameter is always 128 pixels and the terminator is oriented vertically. The images were placed in a 1024^2 grid and Fourier transformed (zero padding increases the frequency sampling). We normalise the square modulus of each FT to one at coordinate origin, multiply it by $f^{1/3}$ and transform back to obtain the scintillation covariance B_ζ modulo a constant coefficient.

Elliptical disk has similarities to the actual Moon's shape, such as finite extend and sharp edge. Ellipse is characterised by its relative diameters δ_x and δ_y, for a circle $\delta_x = \delta_y = 1$. The corresponding filter is

[1] http://home.avvanta.com/~thomast/astro/moonphases.html

$$P_{\rm ell}(\boldsymbol{f}, z) = \left[\frac{2J_1(\pi x)}{\pi x} \right]^2, \quad x = z\theta\sqrt{(f_x \delta_x)^2 + (f_y \delta_y)^2} \quad \text{(B4)}$$

For each Moon's image, we adjust the parameters δ_x and δ_y by matching the equivalent width of the energy spectra of ellipse and image. Then the dependence of these parameters on the Moon's phase (measured by the time t_M from the new Moon in days) is fitted by smooth curves:

$$\begin{aligned} \delta_y &= 1.02 - 0.0004\ (t_M - 14.75)^2, \\ \delta_x &= 0.96/[1 + 0.0172\ (t_M - 14.75)^2]. \end{aligned} \quad \text{(B5)}$$

The scintillation covariance for an ellipse is calculated in the same way as for the true image. The difference normalised by variance, $E = [B_{\rm ell}(\boldsymbol{r}) - B_{\rm Moon}(\boldsymbol{r})]/B_{\rm Moon}(0)$, is a measure of the modeling error. As shown in Fig. B1, the largest errors occur near the first and last quarters. On the other hand, the model is good within ± 5 days from the full Moon. The largest errors are found at the shortest baselines. The full Moon itself does not have a symmetric ACF and the model partially accounts for this: $\delta_x < \delta_y$ at $t_M = 14.75$.

B2 Matrix model

In this model, we approximate the power-spectrum of the Moon's image $|\tilde{A}_{\rm Moon}(\boldsymbol{f}')|^2$ by a 4-th order polynomial in t_M fitted at every pixel of the frequency plane. The normalised dimensionless spatial frequency $\boldsymbol{f}' = \boldsymbol{f}\theta z$ is used, so the model does not depend on the distance z or Moon's diameter θ. The spectra of real images are calculated in the same way as above, but on the 4000^2 pixels grid and with different padding ratio (Moon's diameter 670 pixels or 1/6 of the grid size). Only the central 400^2 pixels of the spectra are retained, meaning that the details smaller than 10 pixels in the original images are smoothed out.

We tried first to fit the polynomials over the full range of Moon's phases (t_M from 2.4 to 24.6), but found that crescent phases strongly influence the result and degrade the accuracy near full Moon. Fitting over the restricted range from 7 to 21 days is done instead. A set of five 400×400 matrices of coefficients is combined with powers of t_M to get the Moon's power spectrum. The difference between scintillation covariances calculated with the matrix model and with the real images does not exceed $\pm 3\%$ of the variance on the time interval ± 6 days around full Moon, $8.5 < t_M < 21$. The maximum difference in covariances between matrix and ellipse models is 8.7%.

B3 Numerical details

Calculation of the WFs is the most time-consuming part of the OTP restoration. We refresh the set of WFs every hour, considering that the change during this interval is small. The Moon's power spectrum for appropriate phase is calculated on a fixed grid (256^2 pixels for ellipse model or 400^2 pixels for matrix model) in the $\boldsymbol{f}'$ space. A grid of 100 points in z from 0.3 m to 10 km with uniform logarithmic sampling is defined. For each z, the frequency sampling in m^{-1} is found, the detector filter $P_{\rm det}(\boldsymbol{f})$ is calculated and multiplied by $P_{\rm Moon}$, turbulence spectrum, and the normalisation coefficient. If the wind speed and direction are known, the $P_{\rm wind}$ is included as well.

The WFs for the set of baselines are computed from the scintillation spectrum by FT. The angle between the vertically oriented baseline and the x-axis (perpendicular to Moon's terminator) is a sum of the parallactic angle and the position angle of the illuminated Moon side. We account for this angle in advance by selecting the f_x axis to be parallel to the baseline and rotating the Moon's spectrum accordingly. The scintillation spectrum is averaged over f_y, the FT is done in one dimension.

APPENDIX C: STATISTICAL ERRORS OF COVARIANCES

The covariances are measured with certain statistical errors related to the properties of the scintillation signal. Here we show that these errors are dominated by the slow scintillation produced in high atmospheric layers and that covariances at all baselines have strongly correlated errors. The terminology becomes confused when we talk about covariances of covariance errors, i.e. 4-th statistical moments of the signal.

Consider the *estimate* of covariance $\hat{B}_{i,j}$ between detectors i and j obtained by averaging the signals over time T. The statistical error of this estimate is related to the covariance between normalised intensity fluctuations ζ_i with a time lag t,

$$B_{ij}(t) = \langle \zeta_i(t' + t)\zeta_j(t') \rangle. \quad \text{(C1)}$$

The signal variance is $\sigma^2 = B_{ii}(0)$. Textbooks give formulae for calculating the variances of statistical estimates. For example, Eq. 8.95 of Bendat & Piersol (1986) reads

$$\begin{aligned} {\rm Var}[\hat{B}_{ij}] &= \frac{1}{T}\int_{-T}^{T} {\rm d}t\ (1 - |t|/T) \\ &\times\ [B_{ii}(t)B_{jj}(t) + B_{ij}(t)B_{ji}(t)]. \end{aligned} \quad \text{(C2)}$$

In the following we assume that the averaging time T is much longer than the signal correlation time. The auto-covariances B_{ii} and B_{jj} are, of course, equal, while $B_{ji}(t) = B_{ij}(-t)$. This simplifies Eq. C2 to

$${\rm Var}[\hat{B}_{ij}] = \frac{1}{T}\int_{-\infty}^{\infty} {\rm d}t\ [B_{ii}^2(t) + B_{ij}(t)B_{ij}(-t)] = \frac{\sigma^4 \tau_{ij}}{T}, \quad \text{(C3)}$$

where we define the time constant τ_{ij} as

$$\tau_{ij} = \sigma^{-4} \int_{-\infty}^{\infty} {\rm d}t\ [B_{ii}^2(t) + B_{ij}(t)B_{ij}(-t)]. \quad \text{(C4)}$$

These time constants depend on the baselines. The time constant for zero baseline $\tau_0 = \tau_{ii}$ is a useful characteristic of the signal variation in one detector. The approximation (C3) is valid for $T \gg \tau_0$. The relative error of the variance measurement is equal to $\sqrt{\tau_0/T}$.

For calculating the error of the reconstructed profile, we also need to know the correlation between the errors at pairs of baselines. The scintillation signal contains an important low-frequency component, therefore *all* covariance errors, even those involving different detector pairs, are correlated.

Let $B = \hat{B}_{ij}$ and $B' = \hat{B}_{kl}$ be two measured covariances, where some indices may coincide. The signals ζ_i are Gaussian, so the fourth moment is expressed by a combination of the second moments,

$$\langle BB' \rangle = \langle \zeta_i\zeta_j \rangle\langle \zeta_k\zeta_l \rangle + \langle \zeta_i\zeta_k \rangle\langle \zeta_j\zeta_l \rangle + \langle \zeta_i\zeta_l \rangle\langle \zeta_j\zeta_k \rangle. \quad \text{(C5)}$$

The correlation (we do not say covariance to avoid confusion) between two errors is

$$\begin{aligned} {\rm Cov}[BB'] &= \langle \Delta B \Delta B' \rangle = \langle BB' \rangle - \langle B \rangle\langle B' \rangle \\ &= \langle \zeta_i\zeta_k \rangle\langle \zeta_j\zeta_l \rangle + \langle \zeta_i\zeta_l \rangle\langle \zeta_j\zeta_k \rangle. \end{aligned} \quad \text{(C6)}$$

Continuing the analogy with Bendat & Piersol (1986), the estimates obtained over a finite time $T \gg \tau_0$ will have the error's correlation

$$\begin{aligned} \mathrm{Cov}[BB'] &= \frac{1}{T}\int_{-\infty}^{\infty} \mathrm{d}t \; [B_{ik}(t)B_{jl}(t) + B_{il}(t)B_{jk}(t)] \\ &= \sigma^4 \tau_{ijkl}/T. \end{aligned} \quad \text{(C7)}$$

The formula (C7) shows that the correlation between the errors of covariances measured at two baselines depends on the temporal covariances at 4 baselines corresponding to all possible pairwise combinations of the 4 detectors involved (where some may coincide).

The temporal covariances $B_{ij}(t)$ can be estimated from the data itself, as done by Hickson, Pfrommer & Crotts (2008) (see Fig. 4). Alternatively, a model of turbulence and wind profiles can be used to get an idea of the expected errors. One such model (double-exponential $C_n^2(h)$ profile, wind speed 20 m/s at 45° angle to the baseline) leads to $\tau_0 = 0.14$ s. All τ_{ij} are longer than 0.085 s and τ_{ijkl} are longer than 0.05 s, showing the strong correlation between measurement errors on all baselines. For accumulation time $T = 60$ s, the relative error of the variance estimate is $\sqrt{\tau_0/T} = 0.05$.

It is clear that the errors of the measured covariances *depend on the scintillation produced by all layers jointly.* Scintillation from high layers is slow and will dominate the measurement errors, even if we are interested only in measuring the low-altitude turbulence with LuSci.

This paper has been typeset from a TEX/ LATEX file prepared by the author.